

# UCSF

## UC San Francisco Previously Published Works

### Title

MR multitasking-based dynamic imaging for cerebrovascular evaluation (MT-DICE): Simultaneous quantification of permeability and leakage-insensitive perfusion by dynamic T1/T2\* mapping

### Permalink

<https://escholarship.org/uc/item/9mf7096m>

### Journal

Magnetic Resonance in Medicine, 89(1)

### ISSN

0740-3194

### Authors

Hu, Zhehao  
Christodoulou, Anthony G  
Wang, Nan  
et al.

### Publication Date

2023

### DOI








10.1002/mrm.29431

### Copyright Information

This work is made available under the terms of a Creative Commons Attribution-NonCommercial-NoDerivatives License, available at <https://creativecommons.org/licenses/by-nc-nd/4.0/>

Peer reviewed

# MR multitasking-based dynamic imaging for cerebrovascular evaluation (MT-DICE): Simultaneous quantification of permeability and leakage-insensitive perfusion by dynamic $T_1/T_2^*$ mapping

Zhehao Hu<sup>1,2,3</sup>  | Anthony G. Christodoulou<sup>2,3</sup>  | Nan Wang<sup>2</sup>  | Yibin Xie<sup>2</sup> | Mark S. Shiroishi<sup>1</sup> | Wensha Yang<sup>4</sup>  | Gabriel Zada<sup>5</sup> | Frances E. Chow<sup>5</sup>  | Ashley S. Margol<sup>6</sup> | Benita Tamrazi<sup>7</sup> | Eric L. Chang<sup>4</sup> | Debiao Li<sup>2,3</sup> | Zhaoyang Fan<sup>1,2,4,8</sup>  

<sup>1</sup>Department of Radiology, University of Southern California, Los Angeles, California, USA

<sup>2</sup>Biomedical Imaging Research Institute, Cedars-Sinai Medical Center, Los Angeles, California, USA

<sup>3</sup>Department of Bioengineering, University of California, Los Angeles, California, USA

<sup>4</sup>Department of Radiation Oncology, University of Southern California, Los Angeles, California, USA

<sup>5</sup>Department of Neurosurgery, University of Southern California, Los Angeles, California, USA

<sup>6</sup>Department of Neuro-oncology, Children's Hospital Los Angeles, Los Angeles, California, USA

<sup>7</sup>Department of Radiology, Children's Hospital Los Angeles, Los Angeles, California, USA

<sup>8</sup>Department of Biomedical Engineering, University of Southern California, Los Angeles, California, USA

## Correspondence

Zhaoyang Fan, Department of Radiology, Keck School of Medicine, University of Southern California, 2250 Alcazar Street, CSC Room 104, Los Angeles, CA, 90033, USA.

Email: [zhaoyang.fan@med.usc.edu](mailto:zhaoyang.fan@med.usc.edu)

## Funding information

National Institutes of Health, Grant/Award Number: R01EB028146

**Purpose:** To develop an MR multitasking-based dynamic imaging for cerebrovascular evaluation (MT-DICE) technique for simultaneous quantification of permeability and leakage-insensitive perfusion with a single-dose contrast injection.

**Methods:** MT-DICE builds on a saturation-recovery prepared multi-echo fast low-angle shot sequence. The k-space is randomly sampled for 7.6 min, with single-dose contrast agent injected 1.5 min into the scan. MR multitasking is used to model the data into six dimensions, including three spatial dimensions for whole-brain coverage, a saturation-recovery time dimension, and a TE dimension for dynamic  $T_1$  and  $T_2^*$  quantification, respectively, and a contrast dynamics dimension for capturing contrast kinetics. The derived pixel-wise  $T_1/T_2^*$  time series are converted into contrast concentration-time curves for calculation of kinetic metrics. The technique was assessed for its agreement with reference methods in  $T_1$  and  $T_2^*$  measurements in eight healthy subjects and, in three of them, inter-session repeatability of permeability and leakage-insensitive perfusion parameters. Its feasibility was also demonstrated in four patients with brain tumors.

**Results:** MT-DICE  $T_1/T_2^*$  values of normal gray matter and white matter were in excellent agreement with reference values (intraclass correlation

coefficients = 0.860/0.962 for gray matter and 0.925/0.975 for white matter ). Both permeability and perfusion parameters demonstrated good to excellent intersession agreement with the lowest intraclass correlation coefficients at 0.694. Contrast kinetic parameters in all healthy subjects and patients were within the literature range.

**Conclusion:** Based on dynamic  $T_1/T_2^*$  mapping, MT-DICE allows for simultaneous quantification of permeability and leakage-insensitive perfusion metrics with a single-dose contrast injection.

#### KEYWORDS

brain tumors, DCE-MR, DSC-MR, MR multitasking, perfusion, permeability

## 1 | INTRODUCTION

Dynamic MR imaging with the administration of a paramagnetic contrast agent (CA) is widely used for assessing brain tissue abnormalities.<sup>1,2</sup> Two common methods are DCE-MR<sup>2</sup> and dynamic susceptibility contrast-enhanced MR (DSC-MR),<sup>3</sup> which track the tissue-level contrast kinetics based on CA-induced  $T_1$ - and  $T_2/T_2^*$ -shortening effects, respectively.<sup>4</sup> Using pharmacokinetic and/or biophysical modeling, DCE-MR can quantify vascular permeability-related properties, such as fractional plasma volume ( $v_p$ ), transfer constant ( $K^{trans}$ ), and fractional extravascular-extracellular volume ( $v_e$ ), and DSC-MR can quantify perfusion-related properties, such as cerebral blood volume (CBV) and cerebral blood flow (CBF). While both permeability and perfusion parameters are often cited for brain tissue assessment, specifically in brain tumors, previous studies have demonstrated that they may provide different but complementary information.<sup>5</sup> Therefore, simultaneous quantification of them may form a more complete basis for disease evaluation and thus improve diagnostic and prognostic performance.<sup>6</sup>

A comprehensive assessment of vascular permeability and perfusion can be achieved by separately acquiring both DCE- and DSC-MR sequences in one imaging session.<sup>7</sup> However, this approach requires additional scan time and, more importantly, multiple doses of CA that potentially creates additional risk to the patients.<sup>8-10</sup> Integrating vascular permeability and perfusion quantification into a single acquisition along with single-dose contrast administration is a more compelling solution. However, both DCE- and DSC-MR signals can be adversely impacted by the opposing relaxation effects (i.e.,  $T_1$  vs.  $T_2/T_2^*$ ). This is non-negligible when blood-brain barrier breaks down and CA extravasates, which is common in brain tumor areas. Several early

methods based on single-echo acquisitions have been published to correct the contrast leakage effect for perfusion imaging.<sup>11-13</sup> The most widely established is the Boxerman-Schmainda-Weisskoff algorithm that estimates the leakage effects by comparing tumor relaxation curves with those in a reference non-enhancing tissue.<sup>11</sup> However, this method suffers from the restrictive assumption of identical hemodynamic properties between the tumor and reference tissue, leading to unreliable estimations of perfusion parameters.<sup>12</sup>

In the past two decades, multi-echo-based methods have been shown to be more reliable for simultaneously estimating DCE- and DSC-MR parameters.<sup>14-16</sup> With multi-echo data, the  $T_1$ -leakage effects caused by blood-brain barrier disruption can be quantified and applied to estimate permeability parameters. After eliminating the  $T_1$ -leakage effects, the remaining  $T_2/T_2^*$ -leakage effects, which typically lead to overestimations of perfusion parameters, can further be mitigated by adopting either gamma-variate fitting or model-based postprocessing approaches.<sup>17-20</sup>

Despite these promising results, multi-echo-based methods continue to face several technical challenges. First, temporal resolution and/or spatial coverage are often sacrificed because of the longer readout time of multiple echoes.<sup>19</sup> However, high temporal resolution is crucial for accurate quantification of DCE- and DSC-MR parameters.<sup>21</sup> Second, most existing techniques linearly transform the dynamic changes in signal intensity to CA concentration for kinetic modeling. However, the linearity approximation may result in considerable quantification errors in tissues with high contrast uptake.<sup>22,23</sup> Third, as the most commonly used acquisition strategy for current multi-echo-based approaches, the gradient-echo EPI pulse sequences suffer from susceptibility-induced signal dropout and imaging distortion. These artifacts appear particularly around air-tissue interfaces,

such as tumor resection cavities, which precludes the quantification of permeability and perfusion in these regions.<sup>4</sup>

MR multitasking is a recently proposed imaging framework that models multiple dynamics in a multidimensional array and exploits the strong spatiotemporal correlation along and across different dimensions to achieve accelerated imaging.<sup>24</sup> To address the aforementioned limitations of existing multi-echo-based methods, in this work, we developed an MR multitasking-based dynamic imaging for cerebrovascular evaluation (MT-DICE) technique for combined DCE- and DSC-MR. With a single 7.6-min scan and a single-dose contrast injection, MT-DICE allows for simultaneous quantification of vascular permeability and leakage-insensitive perfusion based on dynamic  $T_1/T_2^*$  mapping at a 1.2-s temporal resolution.

## 2 | METHODS

### 2.1 | Pulse sequence design

The MT-DICE technique uses a 3D Cartesian acquisition with periodic non-selective saturation recovery (SR) preparations followed by 60 continuous multi-echo FLASH readout segments (Figure 1A). During each segment, six echoes are consecutively collected to capture the  $T_2^*$ -decay effect. Two interleaved subsets of k-space data are collected, as demonstrated in Figure 1B: the high-temporal-resolution training data ( $\mathbf{d}_{tr}$ ) are acquired every five segments at the center encoding line ( $k_y = k_z = 0$ ),<sup>24</sup> and the imaging data ( $\mathbf{d}$ ) are randomly collected with a 3D variable-density Gaussian sampling pattern along both phase- and partition-encoding directions to achieve incoherent k-space undersampling.

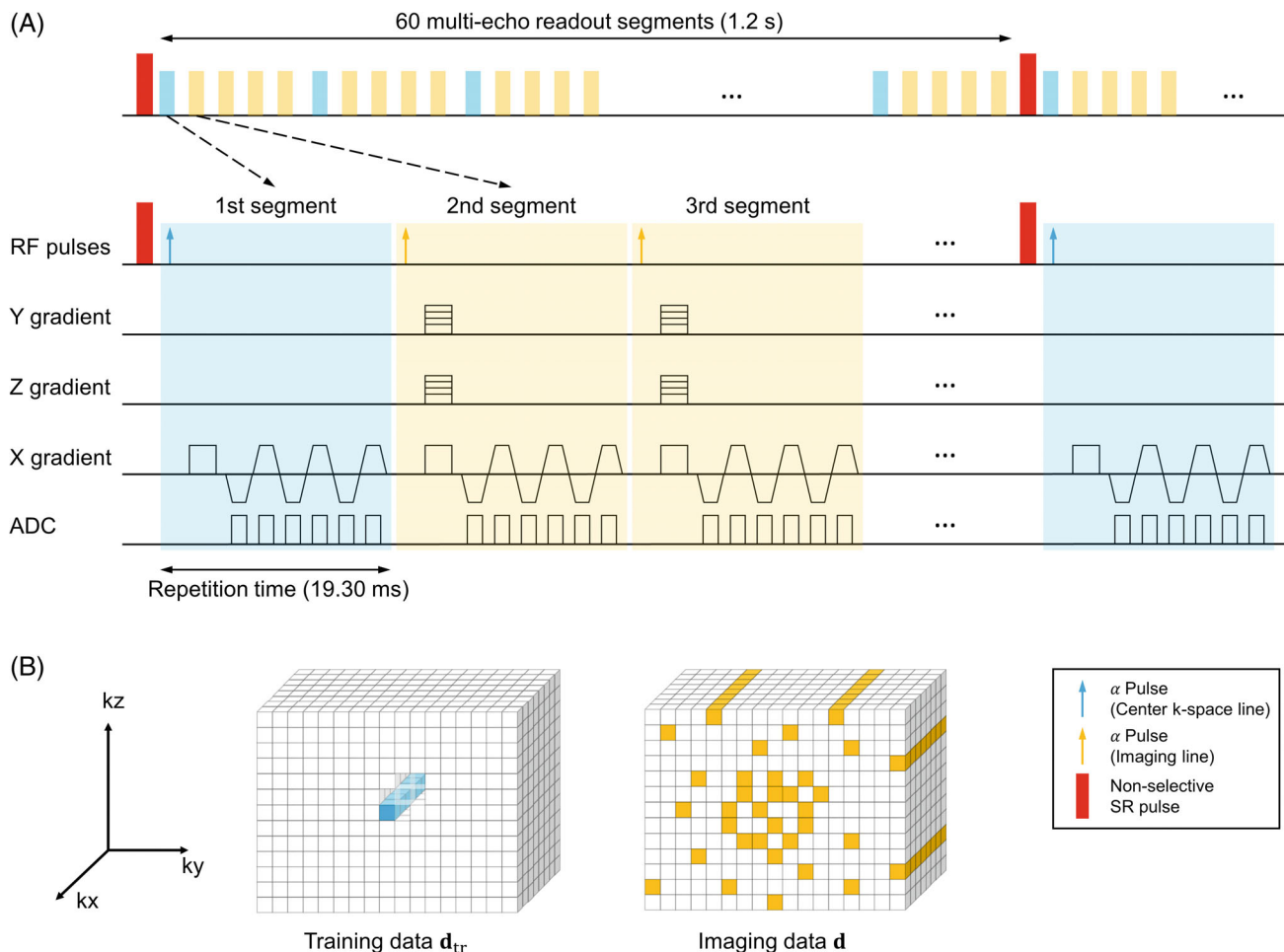


**FIGURE 1** Pulse sequence diagram for the MT-DICE technique and corresponding k-space sampling pattern. A, Non-selective SR pulses were applied every 60 FLASH readout segments. Within each segment, six lines with different TEs were collected at the same k-space location after every alpha pulse. The high-temporal-resolution training data are acquired every four multi-echo readout segments as the low-rank tensor subspace training data. B, Simplified illustration of k-space sampling strategy. The training data were collected at the center encoding line, and the imaging data were collected by Cartesian sampling with randomized reordering with a variable-density Gaussian distribution in  $k_y$  and  $k_z$  directions. MT-DICE, multitasking-based dynamic imaging for cerebrovascular evaluation

## 2.2 | Multidimensional imaging based on MR multitasking

### 2.2.1 | Image model

The MT-DICE method adopts a low-rank tensor (LRT) image model for 6D brain imaging with three spatial dimensions for 3D whole-brain coverage, an SR time dimension and a TE dimension for dynamic T<sub>1</sub> and T<sub>2</sub><sup>\*</sup> quantification, respectively, and a contrast dynamics dimension for capturing contrast kinetics. Specifically, a 6D brain image  $I(\mathbf{r}, \tau, t_E, t)$  is modeled as a four-way multidimensional array (or “tensor”)  $\mathcal{I}$  with elements  $\mathcal{I}_{abcd} = I(\mathbf{r}_a, \tau_b, t_{E,c}, t_d)$ , where the first tensor dimension indexes the set of  $A$  voxel locations  $\{\mathbf{r}_a = [x_a, y_a, z_a]^T\}_{a=1}^A$  and other tensor dimension indexes time dimensions including SR time  $\tau$ , echo time  $t_E$ , and contrast dynamic  $t$ . For example,  $\{\tau_b\}_{b=1}^B$  indexes  $B$  segments within each SR period,  $\{t_{E,c}\}_{c=1}^C$  indexes  $C$  TEs, and  $\{t_d\}_{d=1}^D$  indexes  $D$  contrast dynamic phases. The high correlation between images along and across time dimensions makes  $\mathcal{I}$  an LRT, and is, therefore, partially separable in the following sense:

$$I(\mathbf{r}, \tau, t_E, t) = \sum_{\ell=1}^L u_{\ell}(\mathbf{r}) \varphi_{\ell}(\tau, t_E, t) \quad (1)$$

where  $u_{\ell}(\mathbf{r})$  is the  $\ell$ th of  $L$  spatial basis images, and  $\{\varphi_{\ell}(\tau, t_E, t)\}_{\ell=1}^L$  spans the multidimensional temporal subspace representing a mixture of SR times, multiple TEs, and dynamic contrast changes. Furthermore, in the LRT image model, each  $\varphi_{\ell}(\tau, t_E, t)$  is itself low-rank and can be factorized into basis functions for each time dimension:

$$\varphi_{\ell}(\tau, t_E, t) = \sum_{m=1}^M \sum_{n=1}^N \sum_{p=1}^P c_{\ell mnp} v_m(\tau) w_n(t_E) z_p(t) \quad (2)$$

where  $v_m(\tau)$ ,  $w_n(t_E)$  and  $z_p(t)$  denote the  $m$ th,  $n$ th, and  $p$ th basis functions along the SR time, TE, and contrast dynamics dimensions, respectively; and  $c_{\ell mnp}$  denotes the elements of the core tensor  $C$ . Thus, the image tensor  $\mathcal{I}$  can be expressed as:

$$\mathcal{I} = C \times_1 \mathbf{U} \times_2 \mathbf{V} \times_3 \mathbf{W} \times_4 \mathbf{Z} \quad (3)$$

where  $\times_n$  denotes  $n$ -mode multiplication; the columns of factor matrix  $\mathbf{U}$  contain the spatial basis images and the columns of  $\mathbf{V}$ ,  $\mathbf{W}$ , and  $\mathbf{Z}$  contain the temporal basis functions for each time dimension.<sup>25</sup>

### 2.2.2 | Image reconstruction

There are various low-rank strategies available for reconstruction of the undersampled multidimensional array, either implicitly or explicitly.<sup>24,26–29</sup> MT-DICE, similar to the original MR multitasking work,<sup>24</sup> adopts a mixed strategy that reconstructs the image tensor by sequentially recovering each of its factor matrices. Specifically, in this work, image reconstruction can be divided into four steps:

1. Predetermine the temporal basis functions in  $\mathbf{V}$  (along the SR time dimension). According to the Bloch equations, a predefined training dictionary of physically feasible SR-FLASH signal curves is generated ahead of time with different T<sub>1</sub> and B<sub>1</sub> inhomogeneity values.<sup>24</sup> Basis functions in  $\mathbf{V}$  are extracted from the singular value decomposition of this training dictionary. Temporal basis functions for the TE dimension are not determined in this step due to the complexity of modeling  $B_0$  inhomogeneities and will instead be generated in the following steps.<sup>30</sup>
2. Apply small-scale LRT completion to recover missing elements from the training tensor  $\mathcal{D}_{\text{tr}}$ , which is reshaped from the collected high-temporal-resolution training data  $\mathbf{d}_{\text{tr}}$ . The training tensor  $\mathcal{D}_{\text{tr}}$  covers multiple dynamic contrast combinations throughout the scan; however, it is still highly undersampled since it is impossible to acquire all the image contrast combinations.

$$\hat{\mathcal{D}}_{\text{tr}} = \arg \min_{\mathcal{D}_{\text{tr}(2)} \in \text{range}(\mathbf{V})} \|\mathbf{d}_{\text{tr}} - M(\mathcal{D}_{\text{tr}})\|_2^2 + \lambda \sum_{n=1,3,4} \|\mathbf{D}_{\text{tr}(n)}\|_* \quad (4)$$

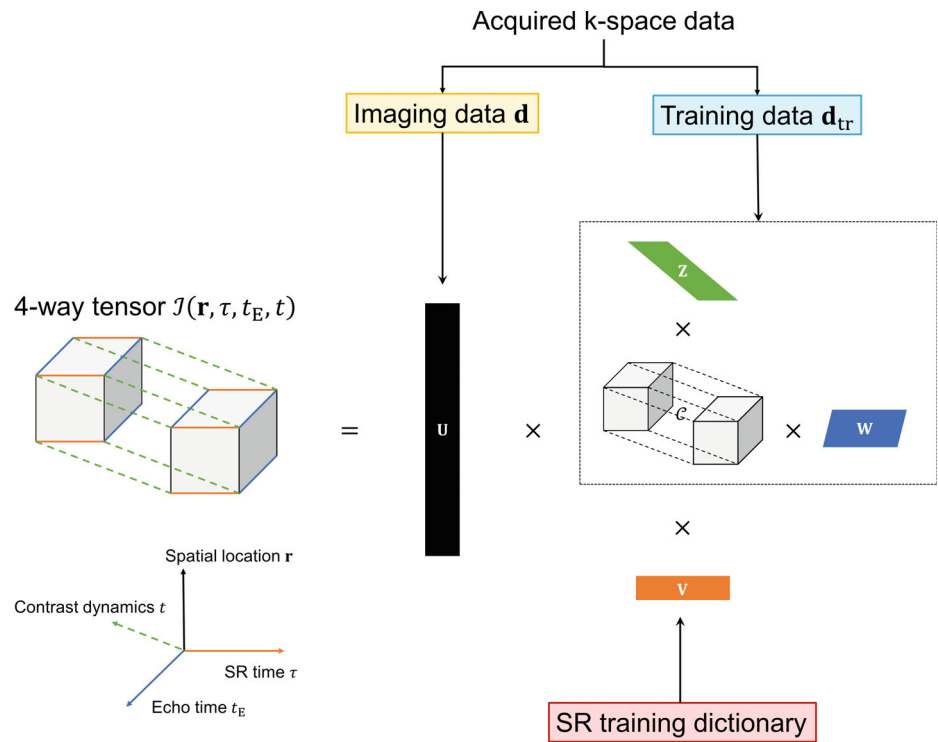
where  $M(\cdot)$  represents the undersampling pattern of the training dataset;  $\mathbf{D}_{\text{tr}(n)}$  denotes the mode- $n$  ( $n = 1, 2, 3, 4$ ) unfolding of the training tensor  $\mathcal{D}_{\text{tr}}$ ;  $\|\cdot\|_*$  is the nuclear norm that promotes low-rankness of each unfolded matrix and  $\lambda$  weights the nuclear norm penalties.

3. Extract temporal basis functions along the TE and contrast dynamics dimensions, namely, columns in  $\mathbf{W}$  and  $\mathbf{Z}$  respectively, as well as the core tensor  $C$  from the high-order singular value decomposition of the completed training tensor  $\hat{\mathcal{D}}_{\text{tr}}$ .
4. Estimate the spatial coefficients  $\mathbf{U}$  by solving the following optimization problem:

$$\hat{\mathbf{U}} = \arg \min_{\mathbf{U}} \|\mathbf{d} - \Omega[\Phi \times_1 \mathbf{F} \mathbf{S} \mathbf{U}]\|_2^2 + R(\mathbf{U}) \quad (5)$$

where  $\Phi = C \times_2 \mathbf{V} \times_3 \mathbf{W} \times_4 \mathbf{Z}$  is the combined temporal factor;  $\Omega(\cdot)$  is the undersampling operator;  $\mathbf{F}$  denotes

**FIGURE 2** Illustration of multiple dimensions of the four-way low-rank tensor image model adopted by MT-DICE and corresponding reconstruction workflow



spatial Fourier transform; and  $S$  denotes the coil sensitivity maps.  $R(\cdot)$  applies the regularization functional, which is chosen as an anisotropic spatial total variation penalty to incorporate compressed sensing into the presented image reconstruction framework.

A diagram of the LRT image model adopted in the proposed MT-DICE and overall reconstruction workflow are shown in Figure 2.

### 2.3 | Dynamic $T_1/T_2^*$ quantification

Voxel-wise dynamic  $T_1/T_2^*$  quantification is performed following image reconstruction. At a given pixel, the multi-echo SR-FLASH signal intensity can be expressed as:

$$S(A, \alpha, B, n, TE, T_1(t), T_2^*(t)) = A \frac{1 - e^{-TR/T_1(t)}}{1 - e^{-TR/T_1(t)} \cos \alpha} \left[ 1 + (B - 1)(e^{-TR/T_1(t)} \cos \alpha)^n \right] e^{-TE/T_2^*(t)} \sin \alpha \quad (6)$$

where amplitude  $A$  absorbs proton density;  $\alpha$  denotes the FLASH flip angle;  $B$  represents saturation factor (ideally zero);  $n$  denotes SR segment index;  $TE$  represents echo times;  $T_1(t)$  and  $T_2^*(t)$  are the dynamic  $T_1/T_2^*$  values over all contrast phases, respectively. All time points were used to fit  $T_1$  and  $T_2^*$  values. For each pixel, we fit for  $A$ ,  $\alpha$ ,  $B$ ,  $T_1(t)$ , and  $T_2^*(t)$  using the lsqnonlin (nonlinear

least-square) solver in MATLAB (R2018a, MathWorks, Natick, MA).

### 2.4 | Estimations of permeability and leakage-insensitive perfusion parameters

Details of parameter estimation are included in the Supporting Information Appendix S1, Section A, and are briefly described here. The  $T_1$ -based CA concentration for tissues of interest was directly derived from the dynamic longitudinal relaxation rates  $R_1(t)$  ( $R_1 = 1/T_1$ ) according to the following equation:

$$C_t^{T_1}(t) = \frac{\Delta R_1(t)}{r_1} = \frac{R_1(t) - R_1(0)}{r_1} \quad (7)$$

where the longitudinal relaxivity  $r_1$  was set to be  $3.6 \text{ L} \cdot \text{mmol}^{-1} \cdot \text{s}^{-1}$  in this work.<sup>31</sup> The resultant  $C_t^{T_1}(t)$  was used to assess DCE-MR related permeability parameters with the two-compartment extended Tofts model.<sup>32</sup> The  $T_1$ -based arterial input function (AIF) was generated by averaging CA concentration time courses from 10 voxels manually selected in regions of the middle cerebral arteries (five voxels from each side). The derived permeability metrics were further adopted to perform leakage correction for the estimations of DSC-MR metrics based on a combined biophysical and pharmacokinetic approach, in which the

change of transverse relaxation rates  $\Delta R_2^*(t)$  ( $R_2^* = 1/T_2^*$ ) can be expressed as the sum of contributions from both the intravascular and the extravascular-extracellular spaces<sup>20</sup>:

$$\Delta R_2^*(t) = C_b^{T_2^*}(t) \otimes \left( r_{2,p}^* R(t) + r_{2,e}^* K^{\text{trans}} \cdot e^{-\frac{k^{\text{trans}}}{v_e} t} \right) \quad (8)$$

where  $C_b^{T_2^*}(t)$  represents  $T_2^*$ -based AIF, which was estimated from the same 10 voxels as generating the  $T_1$ -based AIF with a quadratic model,<sup>33</sup>  $R(t)$  represents the residue function, and  $\otimes$  denotes convolution operation.<sup>34</sup>  $r_{2,p}^*$  and  $r_{2,e}^*$  refer to the transverse relaxivities within the intravascular and extravascular-extracellular spaces, respectively. For technical demonstration,  $r_{2,p}^* = 87 \text{ L} \cdot \text{mmol}^{-1} \cdot \text{s}^{-1}$  and  $r_{2,e}^* = 30 \text{ L} \cdot \text{mmol}^{-1} \cdot \text{s}^{-1}$  were used in this work according to Schmiedeskamp et al.<sup>18</sup> Leakage-insensitive perfusion metrics were then determined from the intravascular component.<sup>35</sup> The MATLAB p-code for the reconstruction and post-processing is available upon request.

## 2.5 | Validation experiments

All imaging experiments were performed on a 3T clinical MR scanner (MAGNETOM Vida; Siemens Healthcare, Erlangen, Germany) with a 20-channel head-neck coil. The in vivo study was approved by the local institutional review board, and all subjects provided written informed consent before participation.

### 2.5.1 | Validation of $T_1/T_2^*$ quantification

#### *Phantom study*

The phantom study was performed on a standard six-vial Calimetrix phantom (Calimetrix, Madison, WI). Each vial has a unique combination of  $T_1/T_2^*$  values that can be used to validate the  $T_1/T_2^*$  mapping accuracy of the developed MT-DICE technique. Reference  $T_1/T_2^*$  maps were obtained with the conventional single-slice inversion-recovery spin-echo and 3D multi-echo gradient-echo sequences, respectively. The detailed imaging protocols of both the reference sequences and MT-DICE are listed in Supporting Information Appendix S1, Section B.  $T_1/T_2^*$  maps of MT-DICE were generated by fitting the reconstructed images voxel-by-voxel with Equation (6). The mean values of each vial were determined from a central slice of the MT-DICE and reference  $T_1/T_2^*$  maps.

#### *Healthy volunteer study*

Eight subjects (aged 24–67y, three females) without known brain abnormalities were recruited. MT-DICE

imaging was performed in an oblique transverse orientation with the following imaging parameters: field-of-view (FOV) =  $216 \times 216 \times 128 \text{ mm}^3$ , spatial resolution =  $1.5 \times 1.5 \times 4.0 \text{ mm}^3$ , pulse TR = 19.30 ms, TEs = 2.46/4.92/7.38/9.84/12.30/17.22 ms (which is enough to generate relatively accurate  $T_2^*$  maps, according to<sup>36</sup> and our pilot study shown in Supporting Information Appendix S1, Section C), SR period (the temporal resolution of dynamic  $T_1/T_2^*$  mapping) is approximately 1.2 s, containing 60 segments at time points varying from 19.30 to 1160 ms, flip angle =  $10^\circ$ , total time = 7.6 min. Single dose (0.1 mmol/kg of body weight) of CA (Gadavist; Bayer Schering Pharma, Berlin, Germany) was administered through antecubital intravenous access 1.5 min into the scan at the rate of 3.0 mL/s, followed by a 20 mL saline flush at the same rate. In addition, single-slice inversion-recovery turbo spin-echo and 3D multi-echo gradient-echo sequences were acquired before MT-DICE to serve as the pre-contrast references for  $T_1/T_2^*$  quantification, respectively. Detailed imaging protocols are shown in Supporting Information Appendix S1, Section D. Two tissue compartments (i.e., gray matter [GM] and white matter [WM]) were selected as regions of interests for  $T_1/T_2^*$  validation on all healthy subjects.

### 2.5.2 | Validation of kinetic parameter estimations

#### *Numerical simulations*

Numerical simulations were performed to validate the accuracy of MT-DICE in the estimation of permeability and leakage-insensitive perfusion metrics. To better simulate the highly heterogeneous environment within brain tumors, a 3D anthropomorphic digital reference brain phantom incorporating a tumor model from a deidentified glioblastoma patient was created.<sup>37–39</sup> The  $T_1/T_2^*$ -based AIFs were generated according to Jaspers et al.<sup>40</sup> and Simpson and He,<sup>41</sup> respectively, with realistic parameters at a 0.1-s temporal resolution. The dynamic  $T_1/T_2^*$  curves were generated for GM, WM and tumor with the detailed parameters listed in Supporting Information Table S3 of the Appendix S1, Section E. Subsequently, the simulated dynamic signal intensities were calculated based on Equation (6) using the downsampled dynamic  $T_1/T_2^*$  curves at a temporal resolution of 1.2 s (as used in the healthy volunteer study protocol). The generated k-space data were first undersampled and then reconstructed using the MT-DICE technique. Dynamic  $T_1/T_2^*$  fitting and kinetic modeling were performed on all slices involving the tumor. In addition to the leakage-insensitive perfusion parameters, the perfusion metrics without leakage correction were derived in the conventional way (Supporting Information Appendix S1, Section A).<sup>35</sup>

### Healthy volunteer study and intersession repeatability analysis

In all eight subjects, permeability and leakage-insensitive perfusion parameters were estimated using the methods described earlier. Three of them returned within 2 wk for a second scan with the same sequence setup as the first scan to assess intersession repeatability. A total of 12 regions of interests were manually drawn at the same locations (the frontal, parietal and occipital regions of the GM and WM of both left and right hemispheres) of each scan.

## 2.6 | Patient pilot study

Four patients (aged 14–60 y, one female) with known brain tumors were recruited, including two patients with glioblastoma, one patient with embryonal tumor with multilayered rosettes, and one patient with meningioma. The MT-DICE sequence was incorporated in a clinical MR study and was acquired during a single dose contrast injection without any preload bolus, using the same protocol as mentioned above. The clinical protocol included pre- and post-contrast  $T_1$ , pre-contrast  $T_2$ -FLAIR, pre-contrast  $T_2$ , and diffusion-weighted imaging.

In each patient, the tumor region was identified on the post-contrast  $T_1$  images. Dynamic  $T_1/T_2^*$  fitting and kinetic modeling were performed on three continuous slices covering the tumor region. Both leakage-insensitive perfusion metrics and those without leakage correction were derived with detailed steps described in Supporting Information Appendix S1, Section A.<sup>35</sup>

## 2.7 | Statistical analysis

All statistical analyses were performed in SPSS version 24 (IBM Corp., Armonk, NY). A  $p$  value  $< 0.05$  was considered to indicate statistical significance.

### 2.7.1 | Validation of $T_1/T_2^*$ quantification

For the phantom study, linear regression analysis, intraclass correlation coefficients (ICCs), Bland–Altman analysis and paired  $t$ -tests were used to assess the  $T_1/T_2^*$  measurement agreement and difference for each vial between MT-DICE and corresponding reference methods. For the healthy volunteer study, the agreements and differences between MT-DICE and corresponding references in pre-contrast  $T_1/T_2^*$  measurement of the GM and WM were evaluated by ICCs and paired  $t$ -tests, respectively.

### 2.7.2 | Validation of kinetic parameter estimations

For the numerical simulation study, the mean, SD, and range of each permeability and leakage-insensitive perfusion parameters for GM, WM and the tumor region were derived. In addition, mean percentage differences between the derived values and the corresponding ground-truth were also calculated. The intersession repeatability of MT-DICE-based  $v_p$ ,  $K^{\text{trans}}$ , CBV, and CBF quantification was evaluated for GM and WM regions of interests separately with the Bland–Altman analysis and ICCs.

## 3 | RESULTS

MT-DICE imaging was performed successfully on all subjects. All image reconstructions were performed off-line on a Linux workstation with a 2.70 GHz dual 12-core Intel Xeon processor equipped with 256 GB RAM and MATLAB. Reconstruction took approximately 1 h while the post-processing (including dynamic  $T_1/T_2^*$  fitting and parameter estimation) took approximately 40 min for each slice.

### 3.1 | Validation of $T_1/T_2^*$ quantification

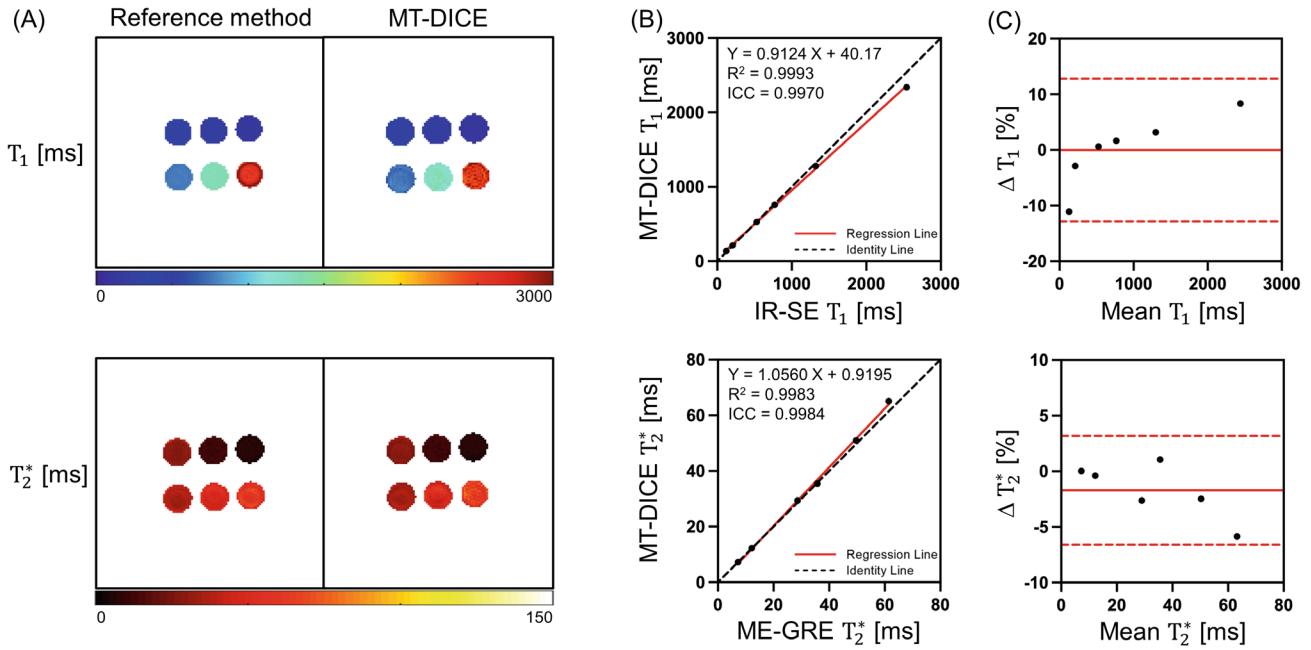
#### 3.1.1 | Phantom study

Figure 3A displays the  $T_1/T_2^*$  maps of the Calimetrix phantom generated by MT-DICE and reference sequences, respectively. There were no significant differences in the  $T_1/T_2^*$  values between the two methods ( $p = 0.247/0.202$ ). Excellent agreements in the  $T_1/T_2^*$  values were observed with  $R^2 = 0.999/0.998$ , and ICC = 0.997/0.998 (Figure 3B). The mean differences were less than 2.5% with limits of agreement both within  $\pm 12\%$  (Figure 3C).

#### 3.1.2 | Healthy volunteer study

With the proposed MT-DICE protocol, there were 380 contrast phases within the entire 7.6-min scan, each of which contains 60 SR times and six TEs. Reconstructed brain images at three representative contrast phases (pre-contrast phase  $t = 20$  s, first-pass phase at  $t = 110$  s, and post-contrast phase at  $t = 420$  s) corresponding to two SR times ( $\tau = 600$  ms and  $\tau = 1200$  ms) and two TEs ( $t_E = 2.46$  ms and  $t_E = 17.22$  ms) are displayed in Figure 4.





**FIGURE 3** Phantom study results. A,  $T_1/T_2^*$  maps of the quantitative six-vial Calimatrix phantom generated by MT-DICE and reference sequences (2D inversion-recovery spin-echo [IR-SE] for  $T_1$  and 3D multi-echo gradient-echo [ME-GRE] for  $T_2^*$  measurements). B, Linear regression analyses and ICC of the  $T_1/T_2^*$  measurements between MT-DICE and reference methods. The black dashed lines represent identity lines ( $y = x$ ), whereas the red solid lines represent regression lines. The  $T_1/T_2^*$  measurements from MT-DICE are in substantial quantitative agreement with reference measurements, as demonstrated by the high  $R^2$  and ICC ( $R^2 = 0.999/0.998$ , and  $ICC = 0.999/0.998$  for  $T_1/T_2^*$ ). C, Bland-Altman analysis shows that their mean differences are less than 2.5% with limits of agreement both within  $\pm 12\%$

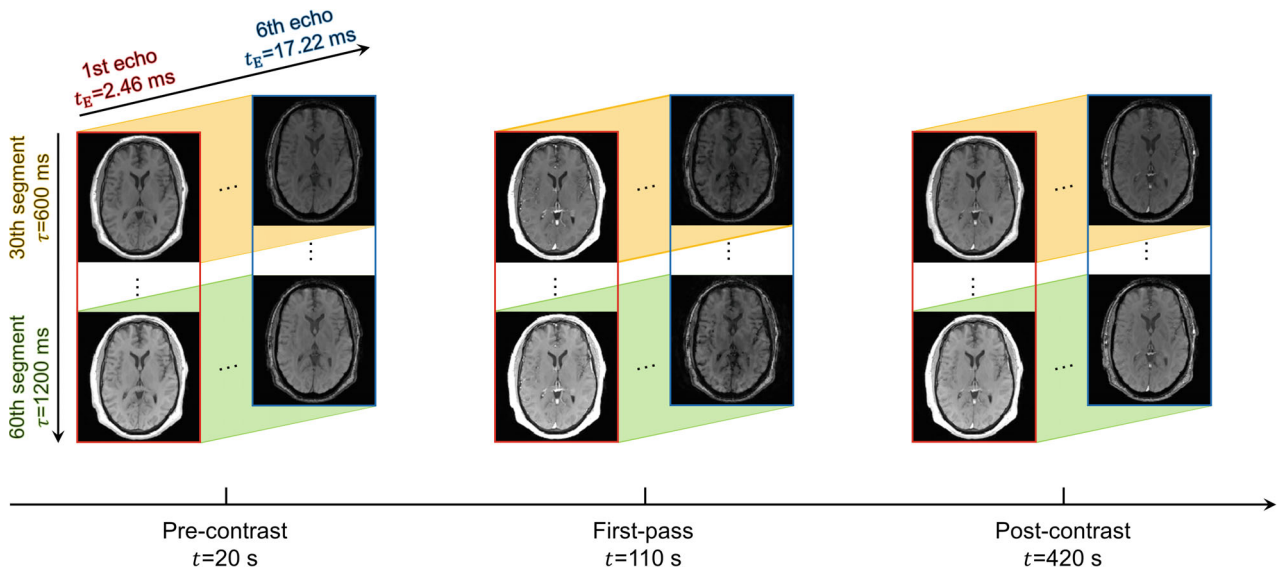


**FIGURE 4** Illustration of multiple time dimensions for MT-DICE and representative images from a healthy volunteer. Multidimensional images along the saturation recovery time dimension  $\tau$ , TE dimension  $t_E$ , and contrast phase dimension  $t$ , can be visualized separately. Example brain images at three representative contrast phases (pre-contrast phase with  $t = 20$  s, first-pass phase with  $t = 110$  s, and post-contrast phase with  $t = 420$  s) corresponding to two representative SR time points ( $\tau = 600$  ms and  $\tau = 1200$  ms) and two representative TEs ( $t_E = 2.46$  ms and  $t_E = 17.22$  ms) are displayed

Figure 5 demonstrates the process of conversion from signal intensity-time curves to  $T_1$ - and  $T_2^*$ -based contrast concentration-time curves using MT-DICE. Figure 5A displays the representative signal intensity-time curves over

all time dimensions (SR time, TE, and contrast dynamics dimensions) generated by averaging the curves of all voxels within a 3-by-3 ROI for blood, GM, and WM, respectively. Figure 5B,C show the corresponding dynamic  $T_1/T_2^*$

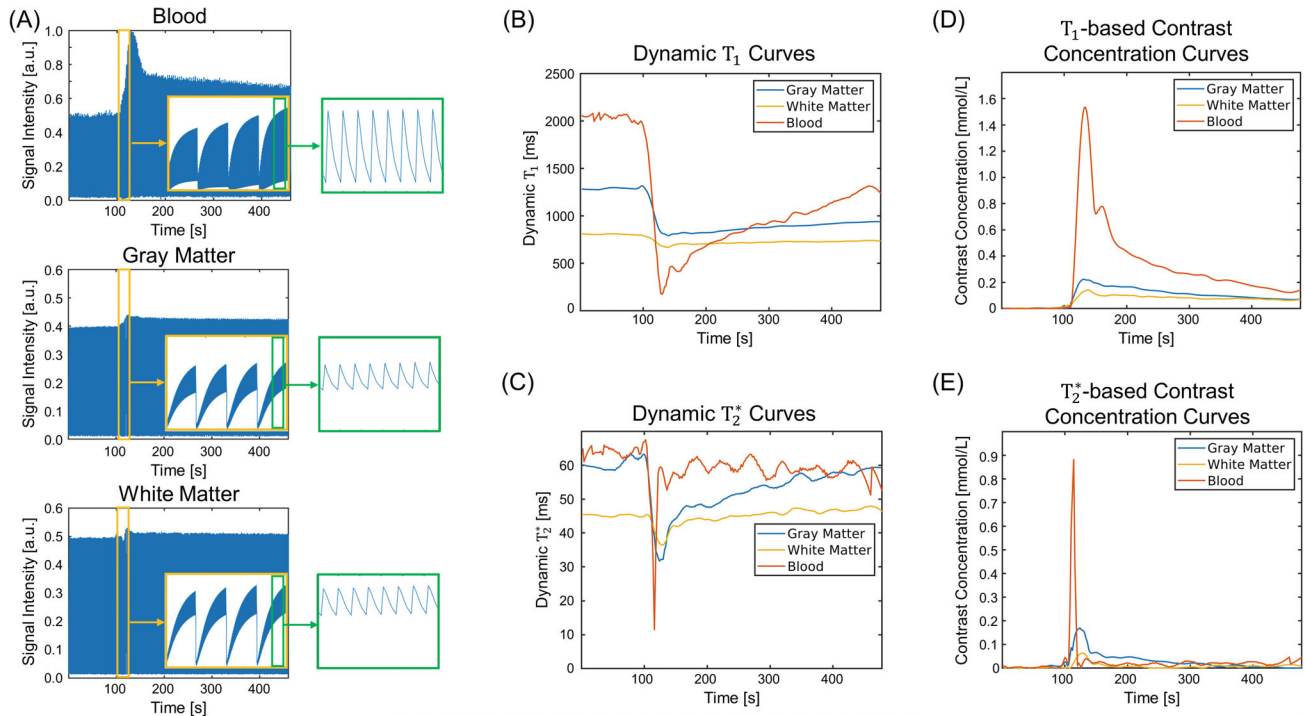


**FIGURE 5** Conversion from signal intensity curves to  $T_1/T_2^*$ -based contrast concentration curves in MT-DICE. A, Representative dynamic signal intensity curves for blood, GM, and WM. The yellow zoomed-in areas show the saturation recovery curves and the green zoomed-in areas show the multi-echo decay curves. B,C, Dynamic  $T_1/T_2^*$  curves. DE,  $T_1/T_2^*$ -based CA concentration curves derived directly from the dynamic  $T_1/T_2^*$  values

curves, and Figure 5D,E display the  $T_1$ - and  $T_2^*$ -based CA concentration-time curves.

Pre-contrast  $T_1/T_2^*$  maps of four representative slices generated by MT-DICE and corresponding reference sequences are displayed for a healthy subject in Figure 6. The parametric maps acquired by MT-DICE were of high image quality and comparable with reference maps, with well-preserved brain tissue structures and contrasts. In quantitative comparisons between MT-DICE and the reference methods (Table 1), all the ICCs of  $T_1/T_2^*$  measurements in GM/WM were within the “excellent” definition range<sup>42</sup> (ICC = 0.860/0.925 and 0.962/0.975 for GM and WM respectively). The  $p$  values of paired  $t$ -tests were 0.219/0.769 and 0.221/0.315 for GM and WM, respectively, indicating insignificant differences between the  $T_1/T_2^*$  values quantified by MT-DICE and the reference methods.

### 3.2 | Validation of kinetic parameter estimations

#### 3.2.1 | Numerical simulations

The simulated dynamic image series at  $\tau = 1200$  ms and  $t_E = 2.46$  ms of one representative slice from the

digital brain phantom, and the ground-truth and MT-DICE derived maps of DCE- and DSC-MR parameters as well as their error maps are shown in Supporting Information Figure S2 of the Appendix S1, Section E. MT-DICE was capable to mitigate contrast leakage effects, which is more evident in CBV quantification, thus leading to smaller mean percentage errors compared to the without leakage correction counterpart (14.39% vs. 18.87%). Table 2 summarizes the quantitative results measured from GM, WM, and the entire tumor model except the necrotic core with the proposed leakage correction algorithm. Different from GM and WM, which were assigned identical kinetic parameters for all voxels during simulation, respectively, the mean, SD, and range of each kinetic parameter are reported for the heterogenous tumor region. The simulation results validated the accuracy of the proposed MT-DICE in kinetic parameter estimations.

#### 3.2.2 | Healthy volunteer study and intersession repeatability analysis

Among all eight healthy volunteers,  $v_p$  [%] ranged 0.092–0.149 for GM and 0.022–0.051 for WM;  $K^{\text{trans}}$  ( $\text{min}^{-1}$ ) ranged 0.006–0.018 for GM and 0.002–0.006 for WM; CBV (ml/100 g) ranged 3.483–4.854 for GM and

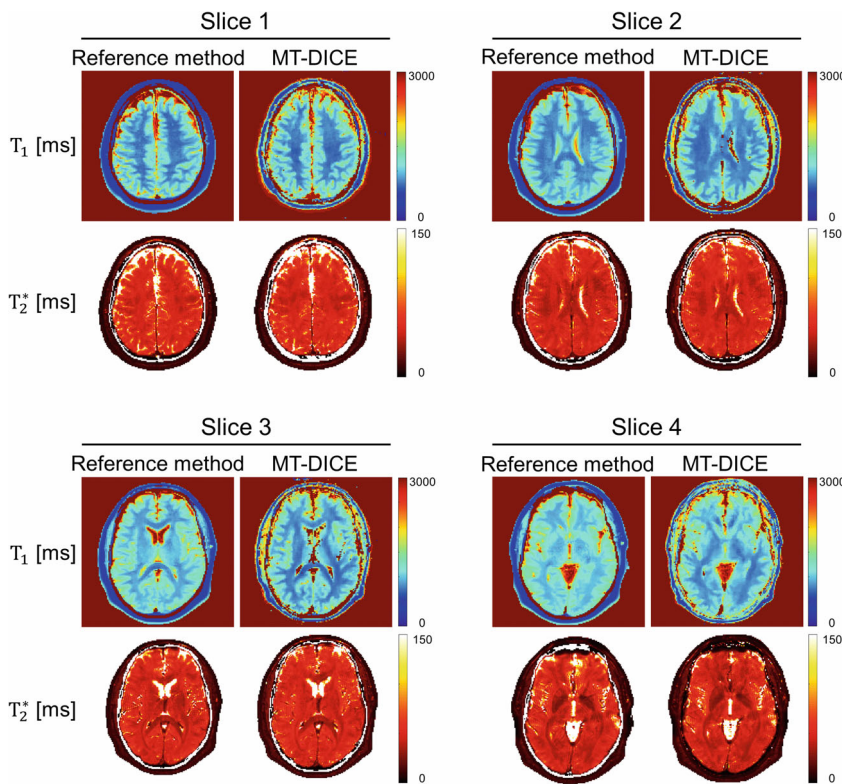


FIGURE 6 Example pre-contrast  $T_1/T_2^*$  generated by MT-DICE and corresponding reference methods on a healthy subject

TABLE 1 Comparison of pre-contrast  $T_1/T_2^*$  measurements of the GM/WM between MT-DICE and corresponding reference methods

|                      |              | MT-DICE (ms)  | Reference method (ms) | ICC [95% CI]         | Paired t-test (p value) |
|----------------------|--------------|---------------|-----------------------|----------------------|-------------------------|
| Pre-contrast $T_1$   | Gray matter  | 1301.4 ± 21.7 | 1291.2 ± 19.9         | 0.860 [0.681, 0.971] | 0.219                   |
|                      | White matter | 781.6 ± 31.6  | 788.0 ± 36.6          | 0.962 [0.823, 0.992] | 0.221                   |
| Pre-contrast $T_2^*$ | Gray matter  | 56.1 ± 1.5    | 56.0 ± 1.4            | 0.925 [0.620, 0.985] | 0.769                   |
|                      | White matter | 39.3 ± 2.4    | 40.5 ± 2.2            | 0.975 [0.941, 0.997] | 0.315                   |

Note:  $T_1/T_2^*$  are presented as mean ± SD.

Abbreviations: CI, confidence interval.

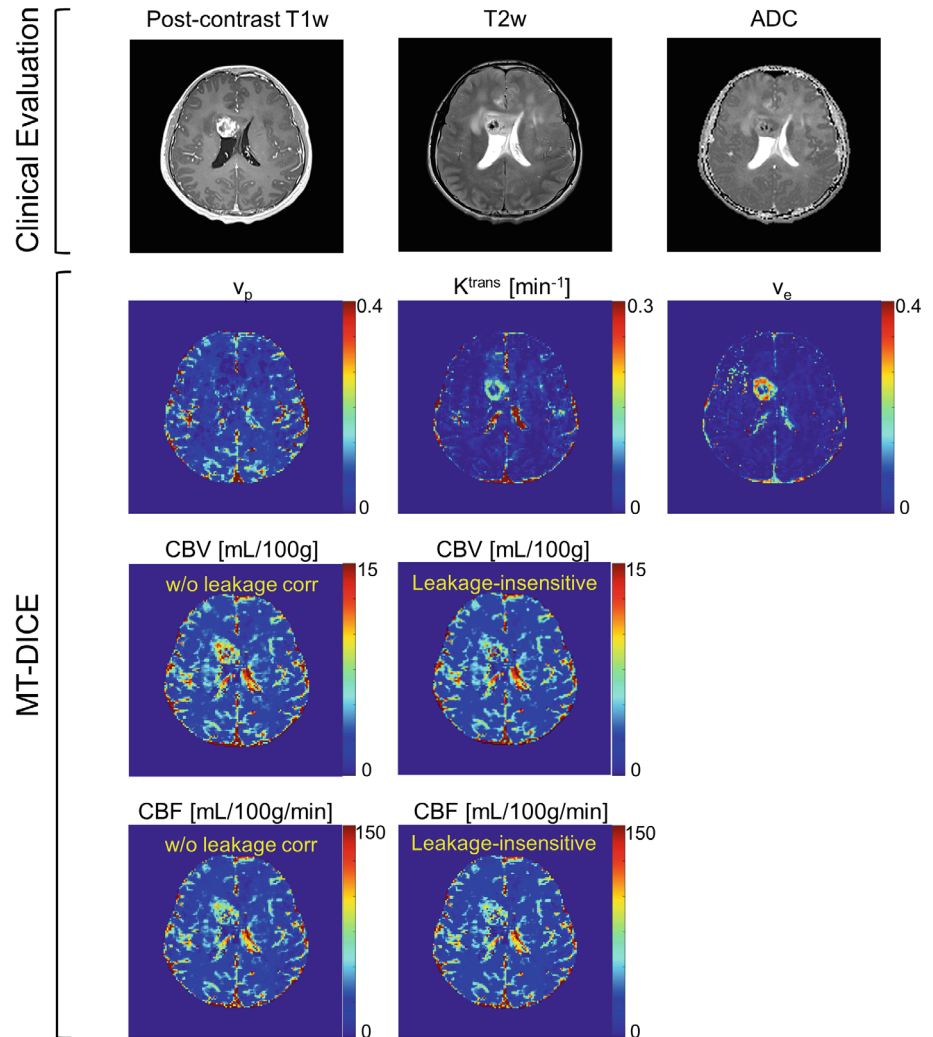
TABLE 2 Ground-truth values, MT-DICE derived values, and corresponding percentage differences of the DCE-MR permeability and leakage-corrected DSC-MR perfusion parameters

|        |  | GM/WM               |                     |                 | Tumor region mean ± std (min – max)     |   |           |
|--------|--|---------------------|---------------------|-----------------|---|---|-----------|
|        |  | GT                  | Derived             | Mean diff       | GT                                      | Derived                                 | Mean diff |
| DCE-MR | $v_p$                                    | 0.0600/<br>0.0300   | 0.0560/<br>0.0276   | 6.67%/<br>8.00% | 0.0280 ± 0.0040<br>(0.0010–0.1000)      | 0.0281 ± 0.0038<br>(0.0025–0.0965)      | 0.36%     |
|        | $K^{\text{trans}}$ ( $\text{min}^{-1}$ ) | 0.0000/<br>0.0000   | 0.0001/<br>0.0001   | –/–             | 0.0780 ± 0.0460<br>(0.0300–0.6000)      | 0.0872 ± 0.0478<br>(0.0372–0.6294)      | 11.58%    |
|        | $v_e$                                    | 0.0000/<br>0.0000   | 0.0001/<br>0.0000   | –/–             | 0.1685 ± 0.0726<br>(0.0010–0.6000)      | 0.1624 ± 0.0694<br>(0.0039–0.5765)      | 3.97%     |
| DSC-MR | CBV (ml/100 g)                           | 3.7500/<br>1.6000   | 3.8470/<br>1.6560   | 2.59%/<br>3.50% | 3.3703 ± 1.9802<br>(0.0200–12.0000)     | 3.8477 ± 2.3769<br>(0.0796–14.2003)     | 14.39%    |
|        | CBF (ml/100 g/min)                       | 40.0000/<br>20.0000 | 38.4300/<br>18.6800 | 3.92%/<br>6.60% | 53.1957 ± 22.8970<br>(12.0000–240.0000) | 58.6976 ± 27.7613<br>(15.1571–276.7812) | 10.54%    |

Note: For tumor region, the reported values are presented as mean ± SD (minimum value – maximum value).

Abbreviations: GT, ground-truth; Mean diff, mean percentage difference.

**FIGURE 7** Representative images of a 14-y-old male patient with ependyoblastoma (World Health Organization grade IV). With MT-DICE, in addition to distinguishing the tumor abnormalities from normal tissues, the heterogeneity within the tumor region could be observed from the vascular permeability maps ( $v_p$ ,  $K^{trans}$ , and  $v_e$ ) and leakage-insensitive perfusion metrics (CBV and CBF). The perfusion parameters without leakage correction are also displayed as comparison



1.429–2.161 for WM; and CBF (mL/100g/min) ranged 41.13–57.56 for GM and 16.15–28.49 for WM. All values were within the literature range.<sup>43,44</sup> Good to excellent intersession repeatability of the selected kinetic parameters in the three subjects were demonstrated with Bland–Altman plots (Supporting Information Figure S3 in Appendix S1, Section F). The ICCs of  $v_p$ ,  $K^{trans}$ , CBV and CBF were 0.822, 0.694, 0.853 and 0.846 respectively in GM, and 0.884, 0.875, 0.727, and 0.750, respectively, in WM.

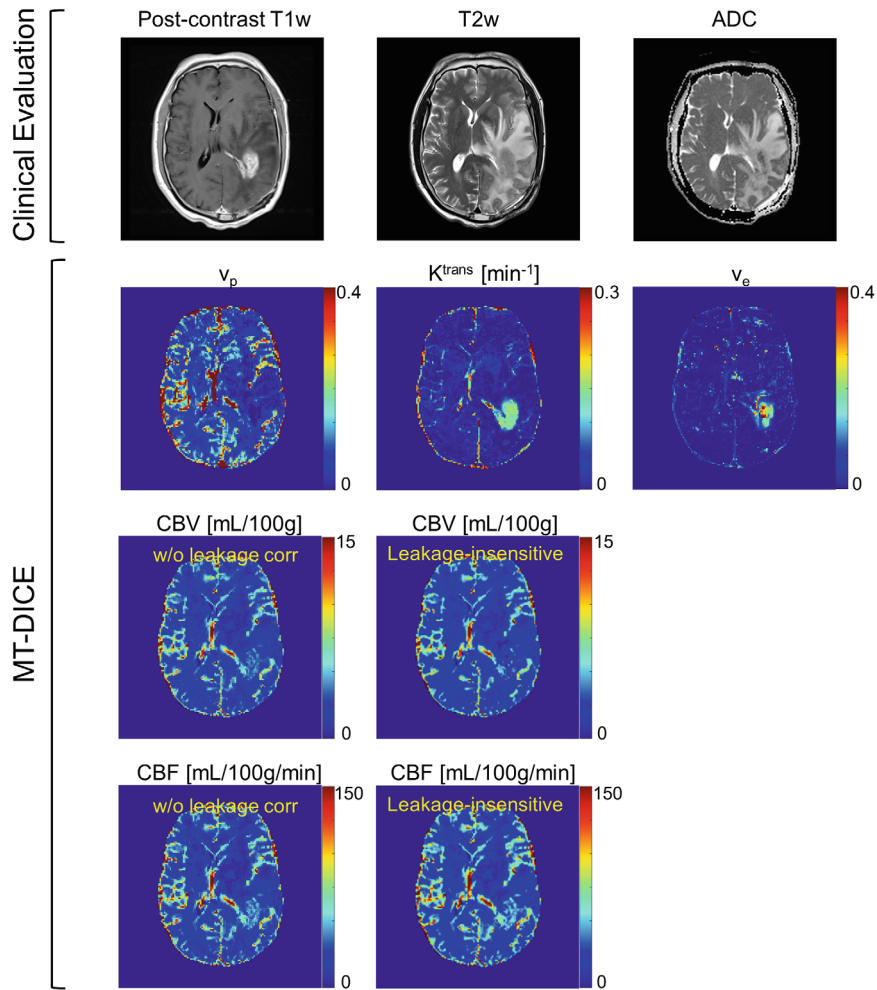
### 3.3 | Patient pilot study

Figure 7 and 8 show the images acquired by MT-DICE and clinical protocols from two representative patients. The patient displayed in Figure 7 was a 14-y-old male diagnosed with embryonal tumor with multilayered rosettes (World Health Organization grade IV). The patient shown in Figure 8 was a 51-y-old male diagnosed with recurrent glioblastoma (World Health Organization grade IV), who underwent radiation therapy prior to this imaging session.

In both patients, the tumor regions were visualized on both the clinical images and quantitative MT-DICE maps. In addition to distinguishing the abnormalities from normal tissues, with the proposed MT-DICE technique, the heterogeneity within the tumor area was observed from the vascular permeability and leakage-insensitive perfusion maps. The perfusion metrics without leakage correction, especially CBV, were slightly higher than their leakage-insensitive counterparts, likely due to the  $T_2^*$  leakage effect.

## 4 | DISCUSSION

In this work, we developed an MT-DICE technique for simultaneous DCE- and DSC-MR quantification with a single-dose injection. With a single 7.6-min scan, the technique provides 3D whole-brain coverage, high temporal resolution of 1.2 s without compromising spatial resolution, dynamic  $T_1/T_2^*$  mapping, and permeability and leakage-insensitive perfusion maps. Hence, a more



**FIGURE 8** Representative images of a 51-y-old male patient with recurrent glioblastoma (World Health Organization grade IV), who underwent radiation therapy prior to the imaging session

comprehensive evaluation of cerebrovascular conditions can be achieved with this technique.

Compared with existing multi-echo-based combined DCE- and DSC-MR techniques, the proposed method has several advantages. First, MT-DICE can achieve a temporal resolution as high as 1.2 s without the compromise in the spatial resolution or coverage. For both DCE- and DSC-MR methods, a sufficient temporal resolution is critical for accurate quantification of kinetic parameters. The general consensus is that a temporal resolution equals to or less than 1.5 s is required for DSC-MR because of the need for adequately capturing the fast passage of CA through tissues.<sup>45</sup> For DCE-MR, the requirement for the temporal resolution is typically less stringent than DSC-MR and is recommended to be less than 5.3 s for brain tumor assessment.<sup>46</sup> However, Li et al. reported that a temporal resolution on the order of 1 s is required to accurately measure AIF, that tends to change more rapidly compared with normal brain tissues.<sup>47</sup> To achieve a sufficiently high temporal resolution, the spatial resolution or coverage may be sacrificed due to the trade-off between spatial and temporal resolutions. An insufficient spatial resolution will lead

to partial volume effects, particularly in the AIF, and can affect the reliability of the estimated parameters.<sup>48</sup> In this work, MT-DICE can achieve a high temporal resolution and a high spatial resolution simultaneously, thanks to the MR multitasking framework which adopts an LRT image model for expedited acquisitions.<sup>24</sup>

Second, MT-DICE quantifies the CA concentration from dynamic  $T_1/T_2^*$  values rather than from  $T_1/T_2^*$ -weighted signal intensities. In most of the existing DCE- and DSC-MR techniques, contrast concentration is derived directly by linear transformation of the dynamic changes in signal intensity. The linearity assumption is valid only when CA concentration is low within the tissue of interests and, thus, may introduce quantification errors in tissues with high CA uptake.<sup>22,49,50</sup> It has been demonstrated that the mapping-based approach provides more accurate estimations compared to the conventional linear approach.<sup>23</sup> In this work, the pre-contrast  $T_1/T_2^*$  fitting accuracy was validated in both phantom and healthy volunteer studies. MT-DICE yielded consistent GM and WM  $T_1/T_2^*$  measurements with excellent agreement with the corresponding reference methods. Post-contrast mapping

results were not assessed in this work since the contrast washout may lead to different  $T_1/T_2^*$  values at different time points. Studies with careful designs are warranted to validate post-contrast  $T_1/T_2^*$  quantification for the blood, for example using a flow phantom or animal model with bolus contrast injection. Furthermore, the dynamic  $T_1$  mapping of MT-DICE not only provides excellent  $T_1$  sensitivity, but also eliminates the necessity of acquiring a separate pre-contrast  $T_1$  map, which is required in conventional DCE-MR methods.<sup>51</sup> This may potentially improve the accuracy of parameter estimations since it gets rid of the interscan subject motion and eliminates the impact of spatial variations in  $B_1$  when using variable flip angles for pre-contrast  $T_1$  mapping.<sup>52,53</sup>

Third, MT-DICE uses a 3D Cartesian acquisition with segmented multi-echo FLASH readouts, which provides vascular permeability and hemodynamic perfusion maps with potentially reduced image distortions. For existing simultaneous DCE- and DSC-MR techniques, single-shot EPI is the most widely used acquisition strategy. However, the major drawback to EPI-based sequences is the geometric distortions due to considerable off-resonance effects during the long readouts required to fully sample the k-space. In addition to adopting advanced EPI acquisitions to reduce the readout length and thereby mitigate distortions, other alternative non-Cartesian readout methods may provide advantages over EPI-based readouts.<sup>4,17</sup> While these non-Cartesian techniques reduce the distortion artifacts induced by EPI, they may lead to other types of image artifacts that could affect the kinetic parameter estimations.<sup>17</sup>

The developed technique is able to simultaneously measure vascular permeability metrics, such as  $v_p$ ,  $K^{\text{trans}}$  and  $v_e$ , together with leakage-insensitive perfusion metrics, such as CBV and CBF. The quantification results from both healthy volunteer and patient groups are generally within the literature range.<sup>43,44</sup> In various cerebrovascular diseases, such as brain tumor and stroke, a disrupted blood-brain barrier results in CA extravasation and may affect the estimated perfusion parameters. Although it has been demonstrated that multi-echo-based acquisitions can elegantly address the  $T_1$ -shortening effects induced by CA extravasation,<sup>17-20,44,54,55</sup> this type of acquisition strategy alone is insufficient for correcting the remaining  $T_2/T_2^*$ -leakage effects. In this study, we adopted a combined biophysical and pharmacokinetic approach which used the derived permeability parameters to address the residual  $T_2^*$ -leakage effect on perfusion estimations.<sup>20</sup> Unlike the method presented by Schmiedeskamp et al.<sup>18</sup> this model avoids sophisticated and multistep parameter fitting, which could potentially improve the robustness of kinetic modeling. It is noted that the  $v_p$  and CBV derived

from MT-DICE in this work were not comparable after accounting for tissue density and the hematocrit level. This is likely due to the fact that the DCE-MR-related parameter  $v_p$  and DSC-MR-related parameter CBV were determined separately through different models based on considerably different MR contrast mechanisms. This finding is in accordance with previous works.<sup>56,57</sup> In the future, we could further optimize the MT-DICE technique by adopting the model proposed by Sourbron et al. which extracts both DCE- and DSC-MR information based on a single two-compartment exchange model.<sup>58</sup>

Our study has several limitations. First, only gradient-echo DSC-MR parameters were available in this work. Given the fact that gradient-echo and spin-echo DSC-MR have different sensitivities on macro- and microvascular perfusion respectively, measurements of both may increase the diagnostic value, which has already been verified in practice.<sup>59,60</sup> In the future, another  $T_2$  time dimension could be added to the LRT image model for dynamic  $T_2$  mapping and used to generate spin-echo DSC-MR parameters.<sup>30,61</sup> Additionally, the  $T_1/T_2^*$  quantification in blood may suffer from the influences of imaging artifacts, such as inflow and partial volume effects, which may potentially lead to quantification errors in AIF. In the future, an optimized MT-DICE protocol with large spatial coverage and high spatial resolution without significantly increasing the total acquisition time would be proposed for better AIF estimation. Third, there is no comparison between the permeability and perfusion parameters generated by MT-DICE and those acquired using conventional DCE- and DSC-MR, respectively. However, it is challenging to validate both DCE- and DSC-MR metrics simultaneously as this requires multiple contrast injections on a single subject. As an alternative, a numerical simulation study was performed in this work to validate the accuracy of MT-DICE in deriving kinetic parameters. Yet, although a tumor model was incorporated to mimic more realistic scenarios, one major limitation of the numerical simulation study is that the susceptibility effects cannot be appropriately modeled without considering field perturbations within heterogenous tumor structures, which may result in some biases for DSC-MR quantification. In the future, studies with careful designs are warranted to directly compare MT-DICE with conventional DCE- and DSC-MR. Last, feasibility of the proposed technique requires further validation on a large patient cohort. More patient cases are required to further validate the capability of MT-DICE in simultaneous permeability and perfusion assessment, and in the meantime, to evaluate whether this technique has better clinical performance in diagnosis, tumor grading, surgical guidance and treatment monitoring compared to conventional methods.

## 5 | CONCLUSIONS


The developed MT-DICE technique allows for simultaneous quantification of permeability and leakage-insensitive perfusion properties with a single-dose contrast injection. With a single 7.6-min scan, it enables 3D whole-brain coverage, high temporal resolution of 1.2 s without compromising spatial resolution, and dynamic  $T_1/T_2^*$  mapping. Our study demonstrates the technical feasibility in healthy subjects and brain tumor patients. Further studies in brain tumors are warranted to validate the clinical utility of this technique.

### ACKNOWLEDGMENT

The authors acknowledge research support from the National Institutes of Health (R01EB028146).


### ORCID

Zhehao Hu  <https://orcid.org/0000-0002-5813-2925>

Anthony G. Christodoulou  <https://orcid.org/0000-0002-9334-8684>

Nan Wang  <https://orcid.org/0000-0002-7616-8083>

Wensha Yang  <https://orcid.org/0000-0002-7274-9454>

Frances E. Chow  <https://orcid.org/0000-0001-5402-2473>

Zhaoyang Fan  <https://orcid.org/0000-0002-2693-0260>

### TWITTER

Zhaoyang Fan  @fan\_zhaoyang

### REFERENCES

- Shiroishi MS, Castellazzi G, Boxerman JL, et al. Principles of  $T_2^*$ -weighted dynamic susceptibility contrast MRI technique in brain tumor imaging. *J Magn Reson Imaging*. 2015;41:296-313.
- Yankeelov TE, Gore JC. Dynamic contrast enhanced magnetic resonance imaging in oncology: theory, data acquisition, analysis, and examples. *Curr Med Imaging Rev*. 2007;3:91-107.
- Willats L, Calamante F. The 39 steps: evading error and deciphering the secrets for accurate dynamic susceptibility contrast MRI. *NMR Biomed*. 2013;26:913-931.
- Quarles CC, Bell LC, Stokes AM. Imaging vascular and hemodynamic features of the brain using dynamic susceptibility contrast and dynamic contrast enhanced MRI. *Neuroimage*. 2019;187:32-55.
- Law M, Yang S, Babb JS, et al. Comparison of cerebral blood volume and vascular permeability from dynamic susceptibility contrast-enhanced perfusion MR imaging with glioma grade. *Am J Neuroradiol*. 2004;25:746-755.
- Seeger A, Braun C, Skardelly M, et al. Comparison of three different MR perfusion techniques and MR spectroscopy for multiparametric assessment in distinguishing recurrent high-grade gliomas from stable disease. *Acad Radiol*. 2013;20:1557-1565.
- Van Cauter S, Peeters R, De Keyser F, Van Gool S, Himmelerich U, Sunaert S. Combining DCE-MRI and DSC-MRI in brain lesions: a feasibility study. Paper presented at: European Congress of Radiology-ECR; March 01–05, 2012; Vienna, Austria.
- Prince MR, Zhang HL, Roditi GH, Leiner T, Kucharczyk W. Risk factors for NSF: a literature review. *J Magn Reson Imaging*. 2009;30:1298-1308.
- McDonald RJ, McDonald JS, Kallmes DF, et al. Intracranial gadolinium deposition after contrast-enhanced MR imaging. *Radiology*. 2015;275:772-782.
- Ramalho J, Castillo M, AlOubaidy M, et al. High signal intensity in globus pallidus and dentate nucleus on unenhanced  $T_1$ -weighted MR images: evaluation of two linear gadolinium-based contrast agents. *Radiology*. 2015;276:836-844.
- Boxerman J, Schmainda K, Weisskoff R. Relative cerebral blood volume maps corrected for contrast agent extravasation significantly correlate with glioma tumor grade, whereas uncorrected maps do not. *Am J Neuroradiol*. 2006;27:859-867.
- Bjornerud A, Sorensen AG, Mouridsen K, Emblem KE.  $T_1$ - and  $T_2^*$ -dominant extravasation correction in DSC-MRI: part I—theoretical considerations and implications for assessment of tumor hemodynamic properties. *J Cereb Blood Flow Metab*. 2011;31:2041-2053.
- Liu HL, Wu YY, Yang WS, Chen CF, Lim KE, Hsu YY. Is Weisskoff model valid for the correction of contrast agent extravasation with combined and effects in dynamic susceptibility contrast MRI? *Med Phys*. 2011;38:802-809.
- Kim E-J, Kim D-H, Lee SH, Huh Y-M, Song H-T, Suh J-S. Simultaneous acquisition of perfusion and permeability from corrected relaxation rates with dynamic susceptibility contrast dual gradient echo. *Magn Reson Imaging*. 2004;22:307-314.
- Newbould RD, Skare ST, Jochimsen TH, et al. Perfusion mapping with multiecho multishot parallel imaging EPI. *Magn Reson Med*. 2007;58:70-81.
- Zaitsev M, D'arcy J, Collins D, Leach M, Zilles K, Shah N. Dual-contrast echo planar imaging with keyhole: application to dynamic contrast-enhanced perfusion studies. *Phys Med Biol*. 2005;50:4491.
- Paulson ES, Prah DE, Schmainda KM. Spiral perfusion imaging with consecutive echoes (SPICE™) for the simultaneous mapping of DSC-and DCE-MRI parameters in brain tumor patients: theory and initial feasibility. *Tomography*. 2016;2:295.
- Schmiedeskamp H, Andre JB, Straka M, et al. Simultaneous perfusion and permeability measurements using combined spin-and gradient-echo MRI. *J Cereb Blood Flow Metab*. 2013;33:732-743.
- Wu J, Saindane AM, Zhong X, Qiu D. Simultaneous perfusion and permeability assessments using multiband multi-echo EPI ( $M_2$ -EPI) in brain tumors. *Magn Reson Med*. 2019;81:1755-1768.
- Stokes AM, Semmineh N, Quarles CC. Validation of a  $T_1$  and  $T_2^*$  leakage correction method based on multiecho dynamic susceptibility contrast MRI using MION as a reference standard. *Magn Reson Med*. 2016;76:613-625.
- Knutsson L, Ståhlberg F, Wirestam R. Aspects on the accuracy of cerebral perfusion parameters obtained by dynamic susceptibility contrast MRI: a simulation study. *Magn Reson Imaging*. 2004;22:789-798.
- Calcagno C, Mani V, Ramachandran S, Fayad ZA. Dynamic contrast enhanced (DCE) magnetic resonance imaging (MRI) of atherosclerotic plaque angiogenesis. *Angiogenesis*. 2010;13:87-99.

23. Wang N, Gaddam S, Wang L, et al. Six-dimensional quantitative DCE MR multitasking of the entire abdomen: method and application to pancreatic ductal adenocarcinoma. *Magn Reson Med*. 2020;84:928-948.
24. Christodoulou AG, Shaw JL, Nguyen C, et al. Magnetic resonance multitasking for motion-resolved quantitative cardiovascular imaging. *Nat Biomed Eng*. 2018;2:215-226.
25. Kolda TG, Bader BW. Tensor decompositions and applications. *SIAM Review*. 2009;51:455-500.
26. Christodoulou AG, Redler G, Clifford B, Liang Z-P, Halpern HJ, Epel B. Fast dynamic electron paramagnetic resonance (EPR) oxygen imaging using low-rank tensors. *J Magn Reson*. 2016;270:176-182.
27. He J, Liu Q, Christodoulou AG, Ma C, Lam F, Liang Z-P. Accelerated high-dimensional MR imaging with sparse sampling using low-rank tensors. *IEEE Trans Med Imaging*. 2016;35:2119-2129.
28. Bustin A, Lima da Cruz G, Jaubert O, Lopez K, Botnar RM, Prieto C. High-dimensionality undersampled patch-based reconstruction (HD-PROST) for accelerated multi-contrast MRI. *Magn Reson Med*. 2019;81:3705-3719.
29. Yaman B, Weingärtner S, Kargas N, Sidiropoulos ND, Akçakaya M. Low-rank tensor models for improved multidimensional MRI: application to dynamic cardiac T1 mapping. *IEEE Trans Comput Imaging*. 2019;6:194-207.
30. Ma S, Wang N, Fan Z, et al. Three-dimensional whole-brain simultaneous T1, T2, and T1 $\rho$  quantification using MR multitasking: method and initial clinical experience in tissue characterization of multiple sclerosis. *Magn Reson Med*. 2021; 85:1938-1952.
31. Pintaske J, Martirosian P, Graf H, et al. Relaxivity of gadopentetate dimeglumine (Magnevist), gadobutrol (Gadovist), and gadobenate dimeglumine (MultiHance) in human blood plasma at 0.2, 1.5, and 3 Tesla. *Invest Radiol*. 2006;41:213-221.
32. Tofts PS, Brix G, Buckley DL, et al. Estimating kinetic parameters from dynamic contrast-enhanced T1-weighted MRI of a diffusable tracer: standardized quantities and symbols. *J Magn Reson Imaging*. 1999;10:223-232.
33. Kjølbj B, Østergaard L, Kiselev V. Theoretical model of intravascular paramagnetic tracers effect on tissue relaxation. *Magn Reson Med*. 2006;56:187-197.
34. Wu O, Østergaard L, Weisskoff RM, Benner T, Rosen BR, Sorensen AG. Tracer arrival timing-insensitive technique for estimating flow in MR perfusion-weighted imaging using singular value decomposition with a block-circulant deconvolution matrix. *Magn Reson Med*. 2003;50:164-174.
35. Straka M, Albers GW, Bammer R. Real-time diffusion-perfusion mismatch analysis in acute stroke. *J Magn Reson Imaging*. 2010;32:1024-1037.
36. Cao T, Ma S, Wang N, et al. Three-dimensional simultaneous brain mapping of T1, T2, T2\* and magnetic susceptibility with MR multitasking. *Magn Reson Med*. 2022;87:1375-1389.
37. Bosca RJ, Jackson EF. Creating an anthropomorphic digital MR phantom—an extensible tool for comparing and evaluating quantitative imaging algorithms. *Phys Med Biol*. 2016;61:974.
38. Cocosco CA, Kollokian V, Kwan RK-S, Pike GB, Evans AC. Brainweb: online interface to a 3D MRI simulated brain database. *NeuroImage*, vol. 5, no. 4, Proceedings of 3rd International Conference on Functional Mapping of the Human Brain, Copenhagen, Denmark. 1997:S425.
39. Collins DL, Zijdenbos AP, Kollokian V, et al. Design and construction of a realistic digital brain phantom. *IEEE Trans Med Imaging*. 1998;17:463-468.
40. Jaspers K, Aerts HJ, Leiner T, et al. Reliability of pharmacokinetic parameters: Small vs. medium-sized contrast agents. *Magn Reson Med*. 2009;62:779-787.
41. Simpson NE, He Z, Evelhoch JL. Deuterium NMR tissue perfusion measurements using the tracer uptake approach: I. optimization of methods. *Magn Reson Med*. 1999;42:42-52.
42. Cicchetti DV. Guidelines, criteria, and rules of thumb for evaluating normed and standardized assessment instruments in psychology. *Psychol Assess*. 1994;6:284.
43. Zhang N, Zhang L, Qiu B, Meng L, Wang X, Hou BL. Correlation of volume transfer coefficient K<sub>trans</sub> with histopathologic grades of gliomas. *J Magn Reson Imaging*. 2012;36:355-363.
44. Bjørnerud A, Emblem KE. A fully automated method for quantitative cerebral hemodynamic analysis using DSC-MRI. *J Cereb Blood Flow Metab*. 2010;30:1066-1078.
45. Welker K, Boxerman J, Kalnin A, Kaufmann T, Shiroishi M, Wintermark M. ASFN recommendations for clinical performance of MR dynamic susceptibility contrast perfusion imaging of the brain. *Am J Neuroradiol*. 2015;36:E41-E51.
46. Heye AK, Culling RD, Hernández MCV, Thrippleton MJ, Wardlaw JM. Assessment of blood-brain barrier disruption using dynamic contrast-enhanced MRI. A systematic review. *Neuroimage Clin*. 2014;6:262-274.
47. Li KL, Buonaccorsi G, Thompson G, et al. An improved coverage and spatial resolution—using dual injection dynamic contrast-enhanced (ICE-DICE) MRI: a novel dynamic contrast-enhanced technique for cerebral tumors. *Magn Reson Med*. 2012;68:452-462.
48. Chen JJ, Smith MR, Frayne R. The impact of partial-volume effects in dynamic susceptibility contrast magnetic resonance perfusion imaging. *J Magn Reson Imaging*. 2005;22:390-399.
49. Wang N, Christodoulou AG, Xie Y, et al. Quantitative 3D dynamic contrast-enhanced (DCE) MR imaging of carotid vessel wall by fast T1 mapping using multitasking. *Magn Reson Med*. 2019;81:2302-2314.
50. Kellman P, Hansen MS, NIELLES-Vallespin S, et al. Myocardial perfusion cardiovascular magnetic resonance: optimized dual sequence and reconstruction for quantification. *J Cardiovasc Magn Reson*. 2017;19:1-14.
51. Landis CS, Li X, Telang FW, et al. Determination of the MRI contrast agent concentration time course in vivo following bolus injection: effect of equilibrium transcytolemmal water exchange. *Magn Reson Med*. 2000;44:563-574.
52. Sung K, Daniel BL, Hargreaves BA. Transmit B1+ field inhomogeneity and T1 estimation errors in breast DCE-MRI at 3T. *J Magn Reson Imaging*. 2013;38:454-459.
53. Sung K, Saranathan M, Daniel BL, Hargreaves BA. Simultaneous T(1) and B(1)(+) mapping using reference region variable flip angle imaging. *Magn Reson Med*. 2013;70:954-961.
54. Quarles CC, Gore JC, Xu L, Yankeelev TE. Comparison of dual-echo DSC-MRI and DCE-MRI-derived contrast agent kinetic parameters. *Magn Reson Imaging*. 2012;30:944-953.
55. Uematsu H, Maeda M. Double-echo perfusion-weighted MR imaging: basic concepts and application in brain tumors for the assessment of tumor blood volume and vascular permeability. *Eur Radiol*. 2006;16:180-186.



56. Alcaide-Leon P, Pareto D, Martinez-Saez E, Auger C, Bharatha A, Rovira A. Pixel-by-pixel comparison of volume transfer constant and estimates of cerebral blood volume from dynamic contrast-enhanced and dynamic susceptibility contrast-enhanced MR imaging in high-grade gliomas. *Am J Neuroradiol.* 2015;36:871-876.
57. Bazyar S, Ramalho J, Eldeniz C, An H, Lee YZ. Comparison of cerebral blood volume and plasma volume in untreated intracranial tumors. *Plos One.* 2016;11:e0161807.
58. Sourbron S, Heilmann M, Walczak C, Vautier J, Schad LR, Volk A. T2\*-relaxivity contrast imaging: first results. *Magn Reson Med.* 2013;69:1430-1437.
59. Schmiedeskamp H, Straka M, Newbould RD, et al. Combined spin-and gradient-echo perfusion-weighted imaging. *Magn Reson Med.* 2012;68:30-40.
60. Speck O, Chang L, DeSilva NM, Ernst T. Perfusion MRI of the human brain with dynamic susceptibility contrast: gradient-echo versus spin-echo techniques. *J Magn Reson Imaging.* 2000;12:381-387.
61. Ma S, Nguyen CT, Han F, et al. Three-dimensional simultaneous brain T1, T2, and ADC mapping with MR multitasking. *Magn Reson Med.* 2020;84:72-88.

## SUPPORTING INFORMATION

Additional supporting information may be found in the online version of the article at the publisher's website.

### Appendix S1. Supporting Information

**Table S1.** The detailed imaging protocols of the reference methods and MT-DICE used in the phantom study are listed below

**Table S2.** The detailed imaging protocols of the reference methods used in the healthy control study are listed below

**Table S3.** Parameters adopted in the numerical simulation study

**Figure S1.** (A) T<sub>2</sub>\* quantification by acquisition with long echo train (left) and short echo train (right), and (B) corresponding Bland–Altman analysis

**Figure S2.** (A) Simulated dynamic image series at  $\tau = 1200$  ms and  $t_E = 2.46$  ms of one representative slice from the constructed digital reference brain phantom. Different phases of dynamic contrast enhancement are clearly visualized from the image series. (B) The ground-truth maps and derived maps of vascular permeability (i.e.,  $v_p$ ,  $K^{\text{trans}}$ , and  $v_e$ ) and perfusion (i.e., CBV and CBF) parameters together with their absolute difference maps. The derived leakage-corrected perfusion metrics were displayed and compared with their non-leakage-corrected counterparts to validate the capability of MT-DICE to estimate leakage-insensitive perfusion parameters

**Figure S3.** Bland–Altman analysis for intersession repeatability assessment on three healthy subjects who were scanned twice on separate days. Four kinetic parameters (i.e.,  $v_p$ ,  $K^{\text{trans}}$ , CBV, and CBF) were measured from 12 regions of interests (frontal, parietal and occipital regions of the gray matter and white matter of both left and right hemispheres from a slice located in the mid brain). Intraclass correlation coefficient (ICC) of each parameter is shown on top of the corresponding Bland–Altman plot

**How to cite this article:** Hu Z, Christodoulou AG, Wang N, et al. MR multitasking-based dynamic imaging for cerebrovascular evaluation (MT-DICE): Simultaneous quantification of permeability and leakage-insensitive perfusion by dynamic T<sub>1</sub>/T<sub>2</sub> mapping. *Magn Reson Med.* 2023;89:161-176. doi: 10.1002/mrm.29431